

Engineering oxygen vacancies in $\text{Na}_2\text{Ti}_3\text{O}_7$ for boosting its catalytic performance in MgH_2 hydrogen storage

Huanhuan Zhang

Henan Polytechnic University

Qianqian Kong

Henan Polytechnic University

Song Hu

Henan Polytechnic University

Dafeng Zhang

Henan Polytechnic University

Haipeng Chen

Luoyang Normal University

Chunbao (Charles) Xu

Western University

Baojun Li (✉ lbjfc1@zzu.edu.cn)

Zhengzhou University <https://orcid.org/0000-0001-8325-3772>

Yanping Fan

Henan Polytechnic University

Baozhong Liu

Henan Polytechnic University

Article

Keywords: Oxygen Vacancy, Hydrogen Storage, MgH_2 , Hydrogen Sorption Kinetics, Catalytic Mechanism.

Posted Date: April 23rd, 2021

DOI: <https://doi.org/10.21203/rs.3.rs-418385/v1>

License:   This work is licensed under a Creative Commons Attribution 4.0 International License.

[Read Full License](#)

Version of Record: A version of this preprint was published at ACS Sustainable Chemistry & Engineering on December 29th, 2021. See the published version at <https://doi.org/10.1021/acssuschemeng.1c06444>.

Abstract

Rational design of high-efficiency catalysts plays a critical role in improving the hydrogen storage performances of the MgH_2 . Herein, flower-like $\text{Na}_2\text{Ti}_3\text{O}_7$ catalyst with rich oxygen vacancies ($\text{Na}_2\text{Ti}_3\text{O}_7\text{-O}_v$) was synthesized from $\text{Ti}_3\text{C}_2\text{-MXene}$ and demonstrated to remarkably enhance the hydrogen storage of MgH_2 . Specifically, with an addition of 5 wt.% $\text{Na}_2\text{Ti}_3\text{O}_7\text{-O}_v$, the initial dehydrogenation temperature of the $\text{MgH}_2 + 5\text{Na}_2\text{Ti}_3\text{O}_7\text{-O}_v$ composite reduced substantially from 287 °C (for MgH_2) to 183 °C. Moreover, the $\text{MgH}_2 + 5\text{Na}_2\text{Ti}_3\text{O}_7\text{-O}_v$ composite exhibited fast hydrogen ab/desorption kinetics and superb reversible hydrogen storage performance with a retention rate of 90.1 % after 10 cycles attributed to the higher structural stability of $\text{Na}_2\text{Ti}_3\text{O}_7\text{-O}_v$. Both experimental and theoretical results confirm that the oxygen vacancies in $\text{Na}_2\text{Ti}_3\text{O}_7\text{-O}_v$ reduce the reaction activation energy during MgH_2 dehydrogenation, hence accounting for the excellent hydrogen sorption kinetics. This work would lead to new design and development of advanced defect-based nano-catalysts for the MgH_2 hydrogen storage system.

Introduction

Hydrogen has been commonly considered as a sustainable and clean energy carrier¹⁻³. Unfortunately, the efficient and safe storage of hydrogen with high gravimetric and volumetric capacity poses a major economical bottleneck for the emerging hydrogen economy^{4,5}. Solid-state hydrogen storage technology, such as metal hydride^{6,7}, metal-organic frameworks⁸⁻¹⁰, or complex hydrides¹¹, has deemed to be a promising method for hydrogen storage due to its high-volume hydrogen storage capacity, safety, free of high pressure and heat insulation vessels¹². Among them, magnesium hydride (MgH_2) has been widely regarded as a most promising hydrogen storage material owing to its high gravimetric hydrogen storage capacity (7.6 wt.%), excellent de/rehydrogenation reversibility, low cost, and environmentally friendly¹³⁻¹⁵. However, the sluggish kinetics of hydrogen ab/desorption of MgH_2 severely limits the practical application of MgH_2 for hydrogen storage¹⁶⁻¹⁸.

Catalyst doping has proven to be an efficient pathway to enhance the reaction kinetics for hydrogen storage in MgH_2 and hence reduce the operating temperatures of the MgH_2 hydrogen storage system¹⁹⁻²¹. Among all catalysts investigated, Ti-based materials are commonly recognized as the best-performing ones and have been widely used to improve the hydrogen storage performances of the MgH_2 system, via significantly reducing the activation energy of de/ab-hydrogenation of MgH_2 while unchanging the enthalpy and entropy in the hydride formation process²². In particular, titanate materials, such as NiTiO_3 ²³, $\text{K}_2\text{Ti}_6\text{O}_{13}$ ²⁴, $\text{TiVO}_{3.5}$ ²⁵, etc., have attracted more attentions in MgH_2 hydrogen storage system. These materials were commonly loaded to MgH_2 via a ball-milling process using sacrificial agents that would in situ decompose into catalytic-inert substance. Thus, the rational design of highly efficient catalysts and development of more stable $\text{Na}_2\text{Ti}_3\text{O}_7$ in the MgH_2 hydrogen storage system would play a vital role in the hydrogen storage system.

As evidently demonstrated in the literature, defect engineering is an effective strategy to expose more active sites and tune the structural regularity and band structure of nanostructured catalysts^{26,27}. The defect could function as active sites for the capture of H₂ molecules and the diffusion of H atoms, which would facilitate MgH₂ activation and result in high catalytic performance in hydrogen storage²⁸. Oxygen vacancy on the Ce₆O₁₁ surface in the Mg₂Ni/Ce₆O₁₁ composite was reported to be a highly efficient site for trapping H₂ molecules²⁹. However, the correlation between defects and catalyst activity, and the mechanism of the defects in hydrogen storage are still not well understood^{30,31,32}. Therefore, it is highly desirable to elucidate the roles of defects in improving the catalytic performance of the MgH₂ hydrogen storage.

In this work, oxygen vacancy-stabilized material structure was designed and the catalytic behavior in MgH₂ hydrogen storage system was realized without catalyst sacrifice. A flower-like Na₂Ti₃O₇ catalyst with rich oxygen vacancies (Na₂Ti₃O₇-O_v) was successfully synthesized from Ti₃C₂ MXene. Considering the abundance of the active sites on the Na₂Ti₃O₇-O_v catalyst, we attempted to introduce it into the MgH₂ system and systematically investigate the dehydrogenation, rehydrogenation, thermodynamics, and kinetics behaviors of the system. The catalytic dehydrogenation was realized due to the existence of oxygen vacancy Na₂Ti₃O₇-O_v catalyst following an excellent hydrogen storage performance. Moreover, first-principles calculation was also performed so as to reveal the roles of Na₂Ti₃O₇-O_v catalyst in reducing the reaction barrier during the dehydrogenation of MgH₂ and improving its hydrogen storage performances.

Results And Discussion

Preparation and Characterization. As illustrated in Fig. 1a, the Na₂Ti₃O₇-O_v catalyst was synthesized via the acid-etching and hydrothermal reaction method. Specifically, the Ti₃C₂ MXene was first prepared by HF etching (Fig. S1). Subsequently, the Na₂Ti₃O₇-O_v was obtained by hydrothermally treating the Ti₃C₂ MXene in a NaOH aqueous solution in the presence of H₂O₂. Figure 1b shows the XRD patterns of the as-prepared Na₂Ti₃O₇-O_v and Na₂Ti₃O₇ samples. Clearly, these peaks can be well assigned to the monoclinic Na₂Ti₃O₇ phase (JCPDS No. 72-0148), which confirms that the treatment did not alter the crystal structure. XPS measurements were performed to investigate the surface chemistry of the fabricated Na₂Ti₃O₇-O_v samples. As illustrated in Fig. S2, a survey-scan spectrum verifies the existence of Na, Ti, and O in the Na₂Ti₃O₇-O_v. In the high-resolution O 1s XPS spectra (Fig. 1c), the peaks at 532.5 eV, 531.0 eV, and 530.2 eV can be attributed to the adsorbed oxygen (O_A), oxygen vacancy (O_V), and lattice oxygen (O_L), respectively³³⁻³⁵. However, in the Na₂Ti₃O₇ sample, the oxygens exist dominantly in the form of O_L (529.9 eV) with a very weak peak of O_V (530.94 eV)^{36,37,38}. Furthermore, oxygen vacancies were also confirmed by the room-temperature electron paramagnetic resonance (EPR) spectroscopy, as shown in Fig. 1d. In Fig. 1d, a strong symmetrical signal peak can be observed in the Na₂Ti₃O₇-O_v sample and the

value of g is 2.003^{39} , while there are no obvious peaks in $\text{Na}_2\text{Ti}_3\text{O}_7$, implying that the electrons should be captured in oxygen vacancies.

SEM image illustrates that the prepared $\text{Na}_2\text{Ti}_3\text{O}_7\text{-O}_v$ presents a flower-like structure with abundance of nanosheets (Fig. 1e) and high specific surface area, which would hence afford a better catalytic property. TEM image (Fig. 1f) further reveals that the nanosheets are ultrathin. The lattice spacings, 0.298 and 0.558 nm, as determined by the high-resolution TEM images of $\text{Na}_2\text{Ti}_3\text{O}_7\text{-O}_v$, are consistent with (003) and (101) planes of $\text{Na}_2\text{Ti}_3\text{O}_7$ (Fig. 1g), respectively. X-ray dispersive analysis (EDS) confirms that Na, Ti, and O elements are distributed uniformly throughout the flower-like structure (Fig. 1h). For comparison, the $\text{Na}_2\text{Ti}_3\text{O}_7$ with different amounts of oxygen vacancies were synthesized and presented in Fig. S3-S6.

De/re-hydrogenation Kinetics Evaluation. To investigate the catalytic performances of $\text{Na}_2\text{Ti}_3\text{O}_7\text{-O}_v$ and $\text{Na}_2\text{Ti}_3\text{O}_7$ catalysts in the MgH_2 hydrogen storage system, MgH_2 was mixed with 5 wt.% catalysts employing a high-speed ball-milling system. The resulting composites are denoted as $\text{MgH}_2 + 5\text{Na}_2\text{Ti}_3\text{O}_7\text{-O}_v$ and $\text{MgH}_2 + 5\text{Na}_2\text{Ti}_3\text{O}_7$, respectively. Firstly, the TPD analysis of these composites was performed. As displayed in Fig. 2a, the initial dehydrogenation temperature of the $\text{MgH}_2 + 5\text{Na}_2\text{Ti}_3\text{O}_7\text{-O}_v$ is $183\text{ }^\circ\text{C}$, significantly lower than that of the $\text{MgH}_2 + 5\text{Na}_2\text{Ti}_3\text{O}_7$ ($205\text{ }^\circ\text{C}$) and the MgH_2 ($287\text{ }^\circ\text{C}$) (Fig. 2b). Impressively, the hydrogen capacity of the $\text{MgH}_2 + 5\text{Na}_2\text{Ti}_3\text{O}_7\text{-O}_v$ (7.3 wt.%) and the $\text{MgH}_2 + 5\text{Na}_2\text{Ti}_3\text{O}_7$ (7.1 wt.%), almost identical to that of the MgH_2 (7.5 wt.%) (Table S1). Obviously, the dehydrogenation capacity of the MgH_2 catalyzed by $\text{Na}_2\text{Ti}_3\text{O}_7$ is lower to $\text{Na}_2\text{Ti}_3\text{O}_7\text{-O}_v$. Thus, the O_v -assisted $\text{Na}_2\text{Ti}_3\text{O}_7$ catalyst presents a higher dehydrogenation capacity in the MgH_2 hydrogen storage system, which could decrease the dosage of $\text{Na}_2\text{Ti}_3\text{O}_7$ and improve the utilization efficiency of MgH_2 . Synchronously, the TPD curves and hydrogen capacity of $\text{Na}_2\text{Ti}_3\text{O}_7$ with different oxygen vacancy amounts were tested and are shown in Fig. S7 and Table S1. The isothermal dehydrogenation profiles of the $\text{MgH}_2 + 5\text{Na}_2\text{Ti}_3\text{O}_7\text{-O}_v$ at different temperatures are shown in Fig. 2c. It can be found that the $\text{MgH}_2 + 5\text{Na}_2\text{Ti}_3\text{O}_7\text{-O}_v$ composite can release 6.9 wt.% hydrogen within 14.0, 6.5, 3.5, and 2.0 min at 220, 240, 260, and $280\text{ }^\circ\text{C}$, respectively. Even at a low temperature of $200\text{ }^\circ\text{C}$, 4.0 wt.% hydrogen could be released from the $\text{MgH}_2 + 5\text{Na}_2\text{Ti}_3\text{O}_7\text{-O}_v$. By contrast, the pure MgH_2 exhibited a sluggish de/re-hydrogenation rate even at a high temperature of $300\text{ }^\circ\text{C}$ (Fig. S8).

To explore the kinetics of hydrogen absorption, the isothermal rehydrogenation of the dehydrogenated $\text{MgH}_2 + 5\text{Na}_2\text{Ti}_3\text{O}_7\text{-O}_v$ were examined at different temperatures (Fig. 2d). As clearly shown in the figure, the $\text{MgH}_2 + 5\text{Na}_2\text{Ti}_3\text{O}_7\text{-O}_v$ reached the maximum hydrogen absorption within 2 min at $200\text{ }^\circ\text{C}$, while it took 10 and 20 min at 150 and $100\text{ }^\circ\text{C}$, respectively. Even when the temperature reduced to $50\text{ }^\circ\text{C}$, the dehydrogenated $\text{MgH}_2 + 5\text{Na}_2\text{Ti}_3\text{O}_7\text{-O}_v$ could absorb 3.6 wt.% hydrogen. As well known, the cycling stability is one of the key crucial parameters for practical application of hydrogen storage materials. To examine the stability of our samples, the cycle durability of the $\text{MgH}_2 + 5\text{Na}_2\text{Ti}_3\text{O}_7\text{-O}_v$ was performed at $280\text{ }^\circ\text{C}$ under 2.2 MPa for hydrogen release and at $200\text{ }^\circ\text{C}$ for hydrogen absorption. As shown in Fig. 2e, the $\text{MgH}_2 + 5\text{Na}_2\text{Ti}_3\text{O}_7\text{-O}_v$ exhibited an excellent reversibility of hydrogen. Specifically, the hydrogen

release capacity of the $\text{MgH}_2 + 5\text{Na}_2\text{Ti}_3\text{O}_7\text{-O}_v$ remained 90.1 % of the original capacity even after 10 cycles (Fig. 2f).

Furthermore, the impact of the $\text{Na}_2\text{Ti}_3\text{O}_7\text{-O}_v$ catalyst on the dehydrogenation kinetics of MgH_2 was also explored at different heating rates (5, 10, 20, and 40 $^\circ\text{C min}^{-1}$). As shown in Fig. S9a and S9b, the decomposition temperature of the $\text{MgH}_2 + 5\text{Na}_2\text{Ti}_3\text{O}_7\text{-O}_v$ is significantly lower than that of the pure MgH_2 at the same heating rate, which is consistent with the analysis results of TPD. The activation energies (E_a) were calculated in accordance to the method as reported in the literature from the slope of Kissinger plots as illustrated in Fig. 2g for both the $\text{MgH}_2 + 5\text{Na}_2\text{Ti}_3\text{O}_7\text{-O}_v$ and pure MgH_2 . The E_a of the $\text{MgH}_2 + 5\text{Na}_2\text{Ti}_3\text{O}_7\text{-O}_v$ was calculated to be 108.16 kJ mol^{-1} , which is much lower than that of the pure MgH_2 (175.34 kJ mol^{-1}), indicating obvious catalytic effect of the $\text{Na}_2\text{Ti}_3\text{O}_7\text{-O}_v$ added to the MgH_2 ^{13,24,25}. To the best of our knowledge, the hydrogen storage performances of the $\text{MgH}_2 + 5\text{Na}_2\text{Ti}_3\text{O}_7\text{-O}_v$ composite are superior to those of the Ti-based MgH_2 systems reported in the literature (Table S2).

To investigate the kinetic mechanism of the $\text{MgH}_2 + 5\text{Na}_2\text{Ti}_3\text{O}_7\text{-O}_v$ system, the normalized isothermal dehydrogenation curves were obtained at 240, 260, and 280 $^\circ\text{C}$ with the $\text{MgH}_2 + 5\text{Na}_2\text{Ti}_3\text{O}_7\text{-O}_v$, as presented in Fig. S9c. It was observed that the $\text{MgH}_2 + 5\text{Na}_2\text{Ti}_3\text{O}_7\text{-O}_v$ released 90 % hydrogen at 240 $^\circ\text{C}$, and it only took 0.80, 1.45, and 3.04 min to reach 50 % of the dehydrogenation capacity at 280, 260, and 240 $^\circ\text{C}$, respectively. Subsequently, the dehydrogenation dynamics were investigated according to the nine kinetic models proposed in our previous report²⁴. It should be noted that $f(\alpha) = A(t/t_{0.5})$, where $t_{0.5}$ is the time when $\alpha = 0.5$ and A is a constant depending on the kinetic model, and $f(\alpha)$ is a term for the reaction rate depending on the reaction mechanism. Plotting the value of $(t/t_{0.5})_{\text{exp}}$ against the $(t/t_{0.5})_{\text{the}}$ value of the R2 model led to good linear lines with slopes close to 1 for the $\text{MgH}_2 + 5\text{Na}_2\text{Ti}_3\text{O}_7\text{-O}_v$ at 280 $^\circ\text{C}$ (Fig. 2h). Based on Jones's investigation, we proposed that the hydrogen desorption of the $\text{MgH}_2 + 5\text{Na}_2\text{Ti}_3\text{O}_7\text{-O}_v$ involves phase-boundary-controlled reactions with a nucleation step occurring virtually instantaneously⁴⁰. Moreover, from the time dependence of kinetic modeling equations $f(\alpha)$ for the $\text{MgH}_2 + 5\text{Na}_2\text{Ti}_3\text{O}_7\text{-O}_v$ at 240, 260, and 280 $^\circ\text{C}$, one can observe that all values of R^2 are greater than 0.98 (Fig. 2i), which confirms the time dependence of the R2 model equation at different temperatures and also suggests the optimal dynamic performance of the $\text{MgH}_2 + 5\text{Na}_2\text{Ti}_3\text{O}_7\text{-O}_v$ in hydrogen ab/desorption.

The thermodynamic properties were investigated by the Pressure-Composition-Isotherm (PCT) measurement technology. As shown in Fig. S10a, the equilibrium pressures of the $\text{MgH}_2 + 5\text{Na}_2\text{Ti}_3\text{O}_7\text{-O}_v$ are 1.997, 3.006, and 5.370 bar at 280, 300, and 320 $^\circ\text{C}$, respectively. Furthermore, Van't Hoff plots (Fig. S10b) were fitted to calculate the decomposition enthalpy change (ΔH) of the $\text{MgH}_2 + 5\text{Na}_2\text{Ti}_3\text{O}_7\text{-O}_v$. As shown, the ΔH value of the $\text{MgH}_2 + 5\text{Na}_2\text{Ti}_3\text{O}_7\text{-O}_v$ was calculated as $67.30 \pm 8.09 \text{ kJ mol}^{-1}$, which is close to the reported literature²⁹. This result confirms that the impact of the addition of $\text{Na}_2\text{Ti}_3\text{O}_7\text{-O}_v$ on the thermodynamic behavior of MgH_2 is minimal.

Hydrogen Storage Mechanism and DFT Analysis. To investigate the catalytic mechanism, XRD, SEM, and TEM measurements of the $\text{MgH}_2 + 5\text{Na}_2\text{Ti}_3\text{O}_7\text{-O}_v$ composite in different states (pristine, dehydrogenated, and rehydrogenated) were carried out. As shown in Fig. 3a, MgH_2 is the main phase in the pristine and the rehydrogenated $\text{MgH}_2 + 5\text{Na}_2\text{Ti}_3\text{O}_7\text{-O}_v$ samples. After dehydrogenation, MgH_2 is completely converted into Mg. Furthermore, XPS results indicate that O_v vacancies are present in the $\text{MgH}_2 + 5\text{Na}_2\text{Ti}_3\text{O}_7\text{-O}_v$ in all three different states. It is worth noting that the peaks of O_v (530.5 eV) for the $\text{MgH}_2 + 5\text{Na}_2\text{Ti}_3\text{O}_7\text{-O}_v$ show a negative shift compared with that of $\text{Na}_2\text{Ti}_3\text{O}_7\text{-O}_v$, likely caused by the mechanical milling. The SEM image and EDS mapping of the $\text{MgH}_2 + 5\text{Na}_2\text{Ti}_3\text{O}_7\text{-O}_v$ after dehydrogenation are presented in Fig. 3c, clearly illustrating that Mg, Na, Ti, and O elements are homogeneously distributed. Moreover, the TEM and high-resolution TEM images confirm that the $\text{Na}_2\text{Ti}_3\text{O}_7\text{-O}_v$ catalyst can stably exist in the $\text{MgH}_2 + 5\text{Na}_2\text{Ti}_3\text{O}_7\text{-O}_v$ in different states, which demonstrates the high stability of the $\text{MgH}_2 + 5\text{Na}_2\text{Ti}_3\text{O}_7\text{-O}_v$ system (Fig. 3d-f and Fig. S11).

DFT calculations were employed to elucidate the roles of $\text{Na}_2\text{Ti}_3\text{O}_7\text{-O}_v$ in catalytic dehydrogenation of MgH_2 . The (101) plane of $\text{Na}_2\text{Ti}_3\text{O}_7\text{-O}_v$ was constructed by DFT calculations. Since the (101) plane in $\text{Na}_2\text{Ti}_3\text{O}_7$ has multiple divulged oxygen and the oxygen can easily form hydroxyl with hydrogen, the surface oxygen is removed in this O_v calculation model, which can keep consistent with the actual experimental situations.

As shown in Fig. 4a, Fig. S12, Table S3, the bonding lengths of Mg-H at the Na-Ti site of the $\text{MgH}_2 + 5\text{Na}_2\text{Ti}_3\text{O}_7\text{-O}_v$ (3.241 Å) is the longest among those at all sites examined (Na, Ti, O and Na-Ti sites), and 0.23 Å longer than that of in the $\text{Na}_2\text{Ti}_3\text{O}_7$ (101) (3.011 Å). Such a long bond length is easy to break, thereby improving the hydrogen storage performances. Moreover, the Na-Ti site in the $\text{MgH}_2 + 5\text{Na}_2\text{Ti}_3\text{O}_7\text{-O}_v$ exhibits much larger adsorption energy ($E_{\text{ads}} = -1.379$ eV) than that of the $\text{MgH}_2 + 5\text{Na}_2\text{Ti}_3\text{O}_7$ ($E_{\text{ads}} = -0.155$ eV), indicating that the $\text{MgH}_2 + 5\text{Na}_2\text{Ti}_3\text{O}_7\text{-O}_v$ presents stronger adsorption of hydrogen toward MgH_2 than that of the $\text{MgH}_2 + 5\text{Na}_2\text{Ti}_3\text{O}_7$. The optimal adsorption structures for MgH_2 molecule at the Na-Ti active sites of the $\text{MgH}_2 + 5\text{Na}_2\text{Ti}_3\text{O}_7\text{-O}_v$ and $\text{MgH}_2 + 5\text{Na}_2\text{Ti}_3\text{O}_7$ with different adsorption sites are presented in Fig. 4b and Fig. S13-S14.

Furthermore, the energy profiles of dissociation and decomposition of MgH_2 molecule on the $\text{MgH}_2 + 5\text{Na}_2\text{Ti}_3\text{O}_7\text{-O}_v$ and $\text{MgH}_2 + 5\text{Na}_2\text{Ti}_3\text{O}_7$ composites were also calculated and are presented in Fig. 4c and Fig. S15, respectively. MgH_2 is firstly adsorbed on the catalyst surface to form an adsorbed species: MgH_2^* . Subsequently, the Mg-H bond in MgH_2^* dissociates into Mg^* and H^* . Finally, H_2 is produced by combing two H^* ²⁸. Clearly, the transition from the initial MgH_2 to TS1 is a rate-limiting step (RLS), where the Gibbs free energy (ΔG) value of the RLS in the $\text{MgH}_2 + 5\text{Na}_2\text{Ti}_3\text{O}_7\text{-O}_v$ was calculated as 0.501 eV, significantly lower than that of the $\text{MgH}_2 + 5\text{Na}_2\text{Ti}_3\text{O}_7$ ($\Delta G = 0.785$, Table S4), which suggests that the $\text{Na}_2\text{Ti}_3\text{O}_7\text{-O}_v$ in the $\text{MgH}_2 + 5\text{Na}_2\text{Ti}_3\text{O}_7$ composite would contribute to a substantial reduction of the reaction barrier during the dehydrogenation of MgH_2 and hence result in greatly improved hydrogen

storage performances. The corresponding schematic diagram is presented in Fig. S16. These results show that $\text{Na}_2\text{Ti}_3\text{O}_7$ has a higher catalytic effect on MgH_2 dissociation. The bonding lengths of Mg-H of MgH_2 molecule and the corresponding adsorption energy (E_{ad}) on the different adsorption site of $\text{Na}_2\text{Ti}_3\text{O}_7$ (101)- $\text{O}_{1\text{v}}$ were also calculated. As expected, the results indicate that O_{v} shows less desorption barrier than $\text{O}_{1\text{v}}$ (Table S5). Additionally, the ΔG of MgH_2 dissociation on the $\text{Na}_2\text{Ti}_3\text{O}_7$ - O_{v} (101) surface (0.501 eV) is also lower than that on Ti (110) surface (0.529 eV) and more detailed results are shown in Fig. S17-S20 and Table S6. Armed with the above results, it can be concluded that $\text{Na}_2\text{Ti}_3\text{O}_7$ derived through defect-engineered strategy can efficiently boost the hydrogen storage performance of MgH_2 ^{41,42}.

Conclusions

In summary, the catalytic dehydrogenation was designed and realized on oxygen vacancy-engineered $\text{Na}_2\text{Ti}_3\text{O}_7$ catalysts with greatly improved catalytic performances in MgH_2 hydrogen storage system. A flower-like $\text{Na}_2\text{Ti}_3\text{O}_7$ catalyst with rich oxygen vacancy was successfully synthesized via a facile method. Experimental and DFT theoretical calculations confirm that the oxygen vacancies on the $\text{Na}_2\text{Ti}_3\text{O}_7$ catalyst can enhance hydrogen storage performances via reducing the Gibbs free energy of MgH_2 dehydrogenation, reducing the initial dehydrogenation temperature of the $\text{MgH}_2 + 5\text{Na}_2\text{Ti}_3\text{O}_7\text{-O}_{\text{v}}$ composite to 183 °C, which is significantly lower than that of the MgH_2 (287 °C). Moreover, the $\text{MgH}_2 + 5\text{Na}_2\text{Ti}_3\text{O}_7\text{-O}_{\text{v}}$ composite exhibits fast kinetics of hydrogen ab/desorption and superb reversible hydrogen storage performance with a retention rate of 90.1 % after 10 cycles. This work provides a promising strategy for designing highly efficient catalysts for hydrogen storage materials.

Methods

Synthesis of Ti_3C_2 . First, Ti_3AlC_2 powders were synthesized according to our previous report.^[20] Specifically, 1.0 g Ti_3AlC_2 was slowly added into 20 mL of 49 wt.% hydrofluoric acid (HF) solution under magnetic stirring at 500 rpm. Subsequently, the above solution was stirred at 60°C in an oil bath under a constant speed. After 24 h, the sample was washed with deionized water until the liquid supernatant reaching neutral. Finally, the Ti_3C_2 MXene was obtained by ultrasonic treatment with ice water for 2 h under Ar atmosphere.

Synthesis of $\text{Na}_2\text{Ti}_3\text{O}_7\text{-O}_{\text{v}}$. $\text{Na}_2\text{Ti}_3\text{O}_7\text{-O}_{\text{v}}$ was synthesized using a hydrothermal method. Specifically, 50 mg of Ti_3C_2 was added into a mixed solution containing 30 mL of 1 M NaOH and 0.68 mL of 30 % H_2O_2 solution following by magnetic stirring for 1 hours. Subsequently, the resulting solution was transferred into a 50 mL Teflon-lined stainless steel autoclave and heated at 180°C for 12 h. Then, the reaction products were washed repeatedly with deionized water and ethyl alcohol. Finally, the $\text{Na}_2\text{Ti}_3\text{O}_7\text{-O}_{\text{v}}$ catalyst was obtained via drying in air in an oven at 60°C for 12 h. For comparison, $\text{Na}_2\text{Ti}_3\text{O}_7$ with different amounts of oxygen vacancies were synthesized by changing the hydrothermal reaction temperature to 160 and 200°C. They are denoted as $\text{Na}_2\text{Ti}_3\text{O}_7\text{-O}_{\text{v}}\text{-160}$ and $\text{Na}_2\text{Ti}_3\text{O}_7\text{-O}_{\text{v}}\text{-200}$, respectively.

Additionally, $\text{Na}_2\text{Ti}_3\text{O}_7$ was also prepared by removing the oxygen vacancies in $\text{Na}_2\text{Ti}_3\text{O}_{7-\text{O}_v}$ by heat treatment at 300°C for 5 h in an air atmosphere.

Synthesis of composite of MgH_2 + 5 wt.% and $\text{Na}_2\text{Ti}_3\text{O}_{7-\text{O}_v}$. The composite of MgH_2 + 5 wt.% $\text{Na}_2\text{Ti}_3\text{O}_{7-\text{O}_v}$ (denote as MgH_2 + $5\text{Na}_2\text{Ti}_3\text{O}_{7-\text{O}_v}$) was prepared by high-speed ball-milling the mixture (95 wt.% commercial MgH_2 + 5 wt.% $\text{Na}_2\text{Ti}_3\text{O}_{7-\text{O}_v}$) at 500 rpm for 12 h under 1.5 MPa H_2 atmosphere. The ball-to-powder ratio was optimized as 60:1. To avoid the friction heat occurring during the ball milling, the ball mill travel and resting time were carefully controlled. Similarly, the MgH_2 + $5\text{Na}_2\text{Ti}_3\text{O}_{7-\text{O}_v-160}$ and MgH_2 + $5\text{Na}_2\text{Ti}_3\text{O}_{7-\text{O}_v-200}$ composites and pure MgH_2 were prepared by the same method as described above. All the experimental processes were handled in an Ar-filled glovebox, and the concentrations of H_2O and O_2 were below 0.1 ppm.

Physical Characterization. The phase compositions of samples were analyzed using X-ray diffraction (XRD, Smart-lab Rigaku) with Cu-K_α radiation (40 kV, 40 mA). An air-sensitive samples holder (Rigaku) covered by an airtight hood accompanying in a glove box was employed to prevent contact with air moisture and oxygen. The morphologies of materials were studied on a scanning electron microscope (SEM, Zeiss Supra 50 VP) and a transmission electron microscope (TEM, JEM-2100). X-ray photoelectron spectra (XPS) were collected on a PHI quantera SXM spectrometer with a monochromatic Al $\text{K}\alpha$ X-ray source (1486.60 eV). The reference C1s peak (284.8 eV) was used to calibrate the binding energies. Raman spectra were recorded on a Renishaw-in via using a 532 nm laser. Differential scanning calorimetry (DSC, STDQ600) measurements were implemented to analyze the decomposition activation energy, where the sample was heated from room temperature to 500°C in 50 mL min^{-1} Ar flow at a heating rate of 5, 10, 20, and $40^\circ\text{C min}^{-1}$, respectively.

De/re-hydrogenation performances. The de/re-hydrogenation behavior and temperature-programmed desorption (TPD) were measured by a Sieverts' apparatus (purchased from Zhejiang University). In a typical test, 0.1 g of the MgH_2 + $5\text{Na}_2\text{Ti}_3\text{O}_7$ composite was loaded into a stainless-steel tube reactor and all the operations were performed in a vacuum glove box. During the TPD experiment, the sample was heated from ambient temperature to 350°C at a heating rate of 3°C min^{-1} . In isothermal experiments, under constant hydrogen pressure of 2.2 MPa the samples were heated to the desired temperature and maintained at the temperature during the following tests.

Declarations

Data availability

All data are available from the authors, please refer to author contributions for specific data sets. Source data are provided as a Source Data file. Source data are provided with this paper.

Acknowledgment

This research is financially supported by the National Natural Science Foundation of China (52071135, 51871090, U1804135, 51671080 and 21805071), Plan for Scientific Innovation Talent of Henan Province (194200510019) and Key Project of Educational Commission of Henan Province (19A150025) as well as the Program of Processing and Efficient Utilization of Biomass Resources of Henan Center for Outstanding Overseas Scientists (GZS2018004).

Author contributions

Prof. B.L., Prof. B.L., H.Z., Q.K., and Prof. Y.F. initiated the project and conceived the experiments. Prof. B.L., Prof. B.L., H.Z., and Q.K., performed the synthesis, characterization and testing of the catalyst. H.Z., Q.K., S. H., D.Z., and H.C. carried out all the experiments and data analysis. H.Z., Q.K. wrote the manuscript together with Prof. B.L., Prof. B.L., Prof. C.X., and Prof. Y.F. gave guidance on the language logic part of the manuscript. All the authors contributed to and commented on this paper.

Competing interests

The authors declare no competing interest.

Additional information

Supplementary information is available for this paper at

Correspondence and requests for materials should be addressed to B.L.

Peer review information Nature Communications thanks the anonymous reviewer(s) for their contribution to the peer review of this work.

Reprints and permission information is available at <http://www.nature.com/reprints>

Publisher's note Springer Nature remains neutral with regard to jurisdictional claims in published maps and institutional affiliations.

References

- 1 Chen, R. et al. Rational design of isostructural 2D porphyrin-based covalent organic frameworks for tunable photocatalytic hydrogen evolution. *Nat. Commun.* **12**, 1354 (2021).
- 2 Zhang, X. et al. A stable low-temperature H₂-production catalyst by crowding Pt on α -MoC. *Nature* **589**, 396-401 (2021).
- 3 Zhang, X. et al. Realizing 6.7 wt% reversible storage of hydrogen at ambient temperature with non-confined ultrafine magnesium hydride. *Energy Environ. Sci.* DOI: 10.1039/D0EE03160G (2021).

- 4 Wu, X. et al. Fast operando spectroscopy tracking in situ generation of rich defects in silver nanocrystals for highly selective electrochemical CO₂ reduction. *Nat. Commun.* **12**, 1354 (2021).
- 5 Shao, Q. et al. Stabilizing and activating metastable nickel nanocrystals for highly efficient hydrogen evolution electrocatalysis. *ACS Nano* **12**, 11625–11631 (2018).
- 6 White, J. L. et al. Identifying the role of dynamic surface hydroxides in the dehydrogenation of Ti-Doped NaAlH₄. *ACS Appl. Mater. Interfaces* **11**, 4930–4941 (2019).
- 7 Wang, Y. R. et al. Heterostructures built in metal hydrides for advanced hydrogen storage reversibility. *Adv. Mater.* **32**, 2002647 (2020).
- 8 Zhou, H. et al. Negative pressure pyrolysis induced highly accessible single sites dispersed on 3D graphene frameworks for enhanced oxygen reduction. *Angew. Chem. Int. Ed.* **59**, 20465–20469 (2020).
- 9 Sun, Y. et al. Modulating electronic structure of metal-organic frameworks by introducing atomically dispersed Ru for efficient hydrogen evolution. *Nat. Commun.* **12**, 1369 (2021).
- 10 Fan, H., et al. MOF-in-COF molecular sieving membrane for selective hydrogen separation. *Nat. Commun.* **12**, 1369 (2021).
- 11 Zheng, X. P. et al. Hydrogen storage performance of HPSB hydrogen storage materials. *Chem. Phys. Lett.* **734**, 136697 (2019).
- 12 Liu, H. Z. et al. Improved hydrogen storage properties of MgH₂ by ball milling with AlH₃: preparations, de/rehydriding properties, and reaction mechanisms. *J. Mater. Chem. A* **1**, 12527–12535 (2013).
- 13 Zhu, W. et al. Using a self-assembled two-dimensional MXene-based catalyst (2D-Ni@Ti₃C₂) to enhance hydrogen storage properties of MgH₂. *ACS Appl. Mater. Interfaces* **12**, 50333–50343 (2020).
- 14 Wang, Y. et al. Core-shell Co@C catalyzed MgH₂: enhanced dehydrogenation properties and its catalytic mechanism. *J. Mater. Chem. A* **2**, 16285–16291 (2014).
- 15 Gao, H. G. et al. Effect of few-layer Ti₃C₂T_x supported nano-Ni via self-assembly reduction on hydrogen storage performance of MgH₂. *ACS Appl. Mater. Interfaces* **12**, 47684–47694 (2020).
- 16 Ding, Z. M. et al. Improve hydrogen sorption kinetics of MgH₂ by doping carbon-encapsulated Iron-Nickel nanoparticles. *J. Alloys Compd.* **843**, 156035 (2020).
- 17 Jangir, M. et al. The enhanced de/re-hydrogenation performance of MgH₂ with TiH₂ additive. *Int. J. Energy Res.* **42**, 1139–1147 (2018).
- 18 Cai, W. P. et al. Effects of carbon nanotubes on the dehydrogenation behavior of magnesium hydride at relatively low temperatures. *J. Mater. Chem. A* **2**, 16369–16372 (2014).

- 19 Zhang, L. T. et al. Two-dimensional ZrCo nanosheets as highly effective catalyst for hydrogen storage in MgH₂. *J. Alloy. Compd.* **805**, 295–302 (2019).
- 20 Fan, Y. P. et al. Two-dimensional MXene/A-TiO₂ composite with unprecedented catalytic activation for sodium alanate. *Catal. Today* **318**, 167–174 (2018).
- 21 Gao, S. C. et al. CNTs decorated with CoFeB as a dopant to remarkably improve the dehydrogenation/rehydrogenation performance and cyclic stability of MgH₂. *Int. J. Hydrogen Energy* **45**, 28964–28973 (2020).
- 22 Zhang, X. L. et al. Empowering hydrogen storage performance of MgH₂ by nanoengineering and nanocatalysis. *Mater. Today Nano* **9**, 100064 (2020).
- 23 Huang, X. et al. Synergistic catalytic activity of porous rod-like TMTiO₃ (TM = Ni and Co) for reversible hydrogen storage of magnesium hydride. *J. Phys. Chem. C* **122**, 27973–27982 (2018).
- 24 Kong, Q. Q. et al. Hamamelis-like K₂Ti₆O₁₃ synthesized by alkali treatment of Ti₃C₂ MXene: catalysis for hydrogen storage in MgH₂. *ACS Sustain. Chem. Eng.* **8**, 4755–4763 (2020).
- 25 Zhang, X. et al. A novel complex oxide TiVO_{3.5} as a highly active catalytic precursor for improving the hydrogen storage properties of MgH₂. *Int. J. Hydrogen Energy* **43**, 23327–23335 (2018).
- 26 Wu, D. Z. et al. Ultralong-lifespan magnesium batteries enabled by the synergetic manipulation of oxygen vacancies and electronic conduction. *ACS Appl. Mater. Interfaces* DOI: 10.1021/acsami.1c00170 (2021).
- 27 Dai, J. et al. Enhanced piezocatalytic activity of Sr_{0.5}Ba_{0.5}Nb₂O₆ nanostructures by engineering surface oxygen vacancies and self-generated heterojunctions. *ACS Appl. Mater. Interfaces* **13**, 7259–7267 (2021).
- 28 Zou, G. D. et al. Synthesis of nanoflower-shaped MXene derivative with unexpected catalytic activity for dehydrogenation of sodium alanates. *ACS Appl. Mater. Interfaces* **9**, 7611–7618 (2017).
- 29 Liu, P. et al. In-situ synthesis of Mg₂Ni-Ce₆O₁₁ catalyst for improvement of hydrogen storage in magnesium. *Chem. Eng. J.* **385**, 123448 (2020).
- 30 Wang, L. W. et al. Defect-rich adhesive molybdenum disulfide/rGO vertical heterostructures with enhanced nanozyme activity for smart bacterial killing application. *Adv. Mater.* **32**, 2005423 (2020).
- 31 Zhu, J. Y. et al. Defect-engineered graphene for high-energy and high-power-density supercapacitor devices. *Adv. Mater.* **28**, 7185–7192 (2016).

- 32 Jiang, S. H. et al. Promoting formation of oxygen vacancies in two-dimensional cobalt-doped ceria nanosheets for efficient hydrogen evolution. *J. Am. Chem. Soc.* **142**, 6461–6466 (2020).
- 33 Zhang, B. B. et al. Ultrathin FeOOH nanolayers with abundant oxygen vacancies on BiVO₄ photoanodes for efficient water oxidation. *Angew. Chem. Int. Ed.* **57**, 2248–2252 (2018).
- 34 Zhang, D. Z. et al. Ultrasensitive H₂S gas detection at room temperature based on copper oxide/molybdenum disulfide nanocomposite with synergistic effect. *Sens. Actuators B Chem.* **287**, 346–355 (2019).
- 35 Fan, W. J. et al. Boosting the photocatalytic performance of (001) BiOI: enhancing donor density and separation efficiency of photogenerated electrons and holes. *Chem. Commun.* **52**, 5316–5319 (2016).
- 36 Zhong, W. et al. MXene-derivative pompon-like Na₂Ti₃O₇@C anode material for advanced sodium ion batteries. *Chem. Eng. J.* **378**, 122209 (2019).
- 37 Vattikuti, S. V. P. et al. Graphitic carbon Nitride/Na₂Ti₃O₇/V₂O₅ nanocomposite as a visible light active photocatalyst. *Ceram. Int.* **46**, 18287–18296 (2020).
- 38 Li, Q. et al. Dandelion-like Mn/Ni Co-doped CoO/C hollow microspheres with oxygen vacancies for advanced lithium storage. *ACS Nano* **13**, 11921–11934 (2019).
- 39 Guan, S. Y. et al. Oxygen vacancy excites Co₃O₄ nanocrystals embedded into carbon nitride for accelerated hydrogen generation. *Appl. Catal. B Environ.* **269**, 118775 (2020).
- 40 Zhang, Y. W. et al. Synergistic effect of LiBH₄ and LiAlH₄ additives on improved hydrogen storage properties of unexpected high capacity magnesium hydride. *J. Phys. Chem. C* **122**, 2528–2538 (2018).
- 41 Zhang, L. T. et al. Enhanced hydrogen storage properties of MgH₂ with numerous hydrogen diffusion channels provided by Na₂Ti₃O₇ nanotubes. *J. Mater. Chem. A* **5**, 6178–6185 (2017).
- 42 Zhang, L. T. et al. A striking catalytic effect of facile synthesized ZrMn₂ nanoparticles on the de/rehydrogenation properties of MgH₂. *J. Mater. Chem. A* **7**, 5626–5634 (2019).

Figures

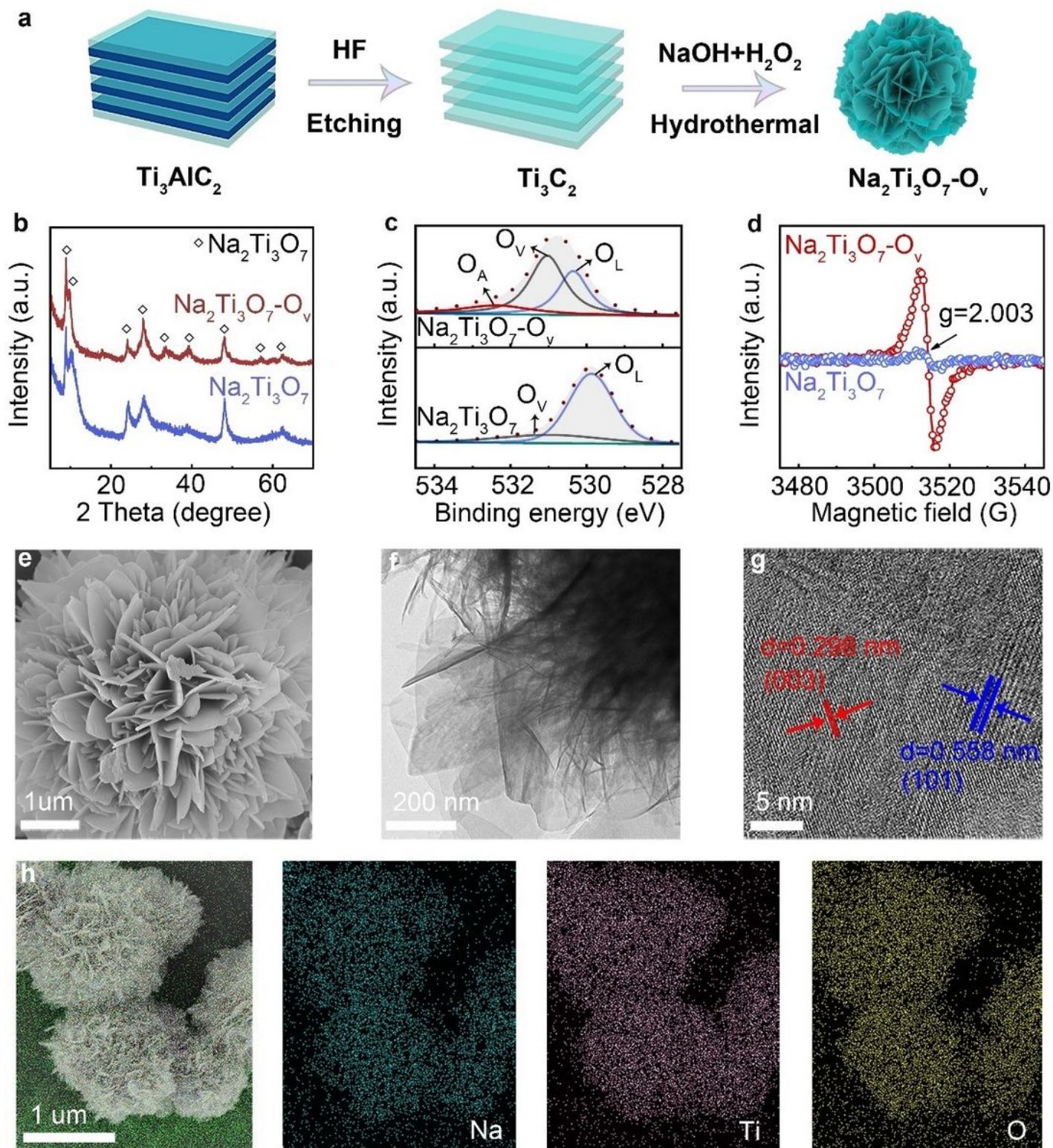


Figure 1

The morphology and structure characterizations of $\text{Na}_2\text{Ti}_3\text{O}_7\text{-O}_v$: (a) Schematic illustration of the material process; (b) XRD patterns; (c) High-resolution O 1s XPS spectra; (d) EPR spectra; (e) SEM image; (f, g) TEM images; (h) High-resolution SEM image; (i) SEM image and the corresponding EDS mapping.

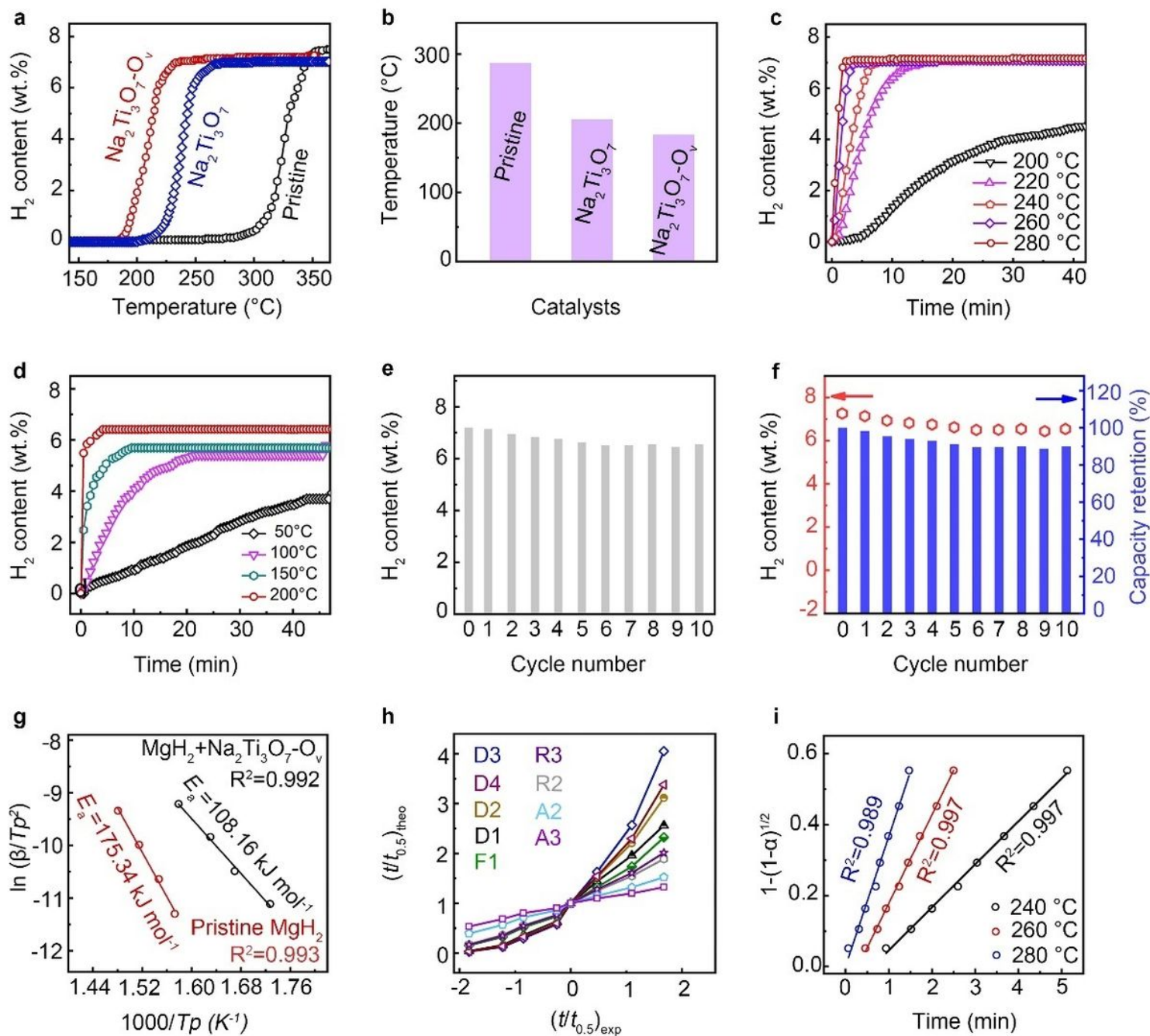


Figure 2

Hydrogen storage performance characterizations of MgH₂ in the presence of Na₂Ti₃O₇-O_v and Na₂Ti₃O₇ catalysts: (a) TPD curves; (b) The onset of dehydrogenation temperature histogram comparison plots; (c) Isothermal dehydrogenation profiles of the MgH₂ + 5Na₂Ti₃O₇-O_v; (d) Isothermal hydrogenation profiles at different temperatures of the dehydrogenated MgH₂ + 5Na₂Ti₃O₇-O_v; (e, f) Cycle performance of the dehydrogenation (280 °C) under 2.2 MPa and the corresponding hydrogen content and capacity retention rate for the MgH₂ + 5Na₂Ti₃O₇-O_v; (g) Kissinger plots of the MgH₂ + 5Na₂Ti₃O₇-O_v and the pure MgH₂; (h) $(t/t_{0.5})_{\text{theo}}$ vs $(t/t_{0.5})_{\text{exp}}$ of the MgH₂ + 5Na₂Ti₃O₇-O_v at 280 °C for various kinetic models; (i) Time dependence of kinetic model equations $f(\alpha)$ for the MgH₂ + 5Na₂Ti₃O₇-O_v at different temperatures.

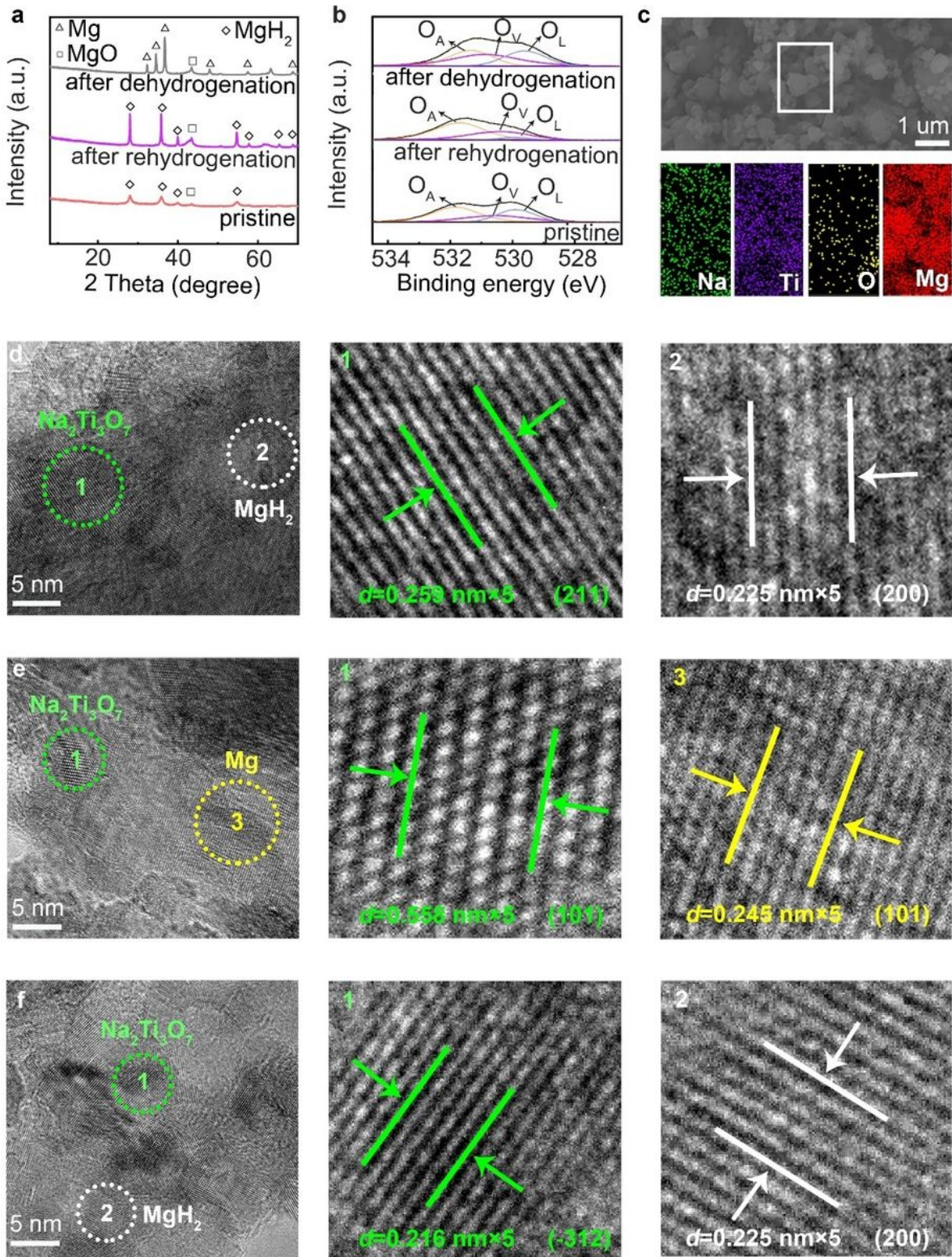


Figure 3

Morphology and structure characterizations of the MgH₂+5Na₂Ti₃O₇-O_v composite in different states: (a) XRD patterns; (b) High-resolution XPS spectra; (c) SEM image and EDS mapping of the MgH₂ + 5Na₂Ti₃O₇-O_v after dehydrogenation. HRTEM images of the (d) pristine, (e) dehydrogenated, and (f) rehydrogenated MgH₂ + 5Na₂Ti₃O₇-O_v composite.

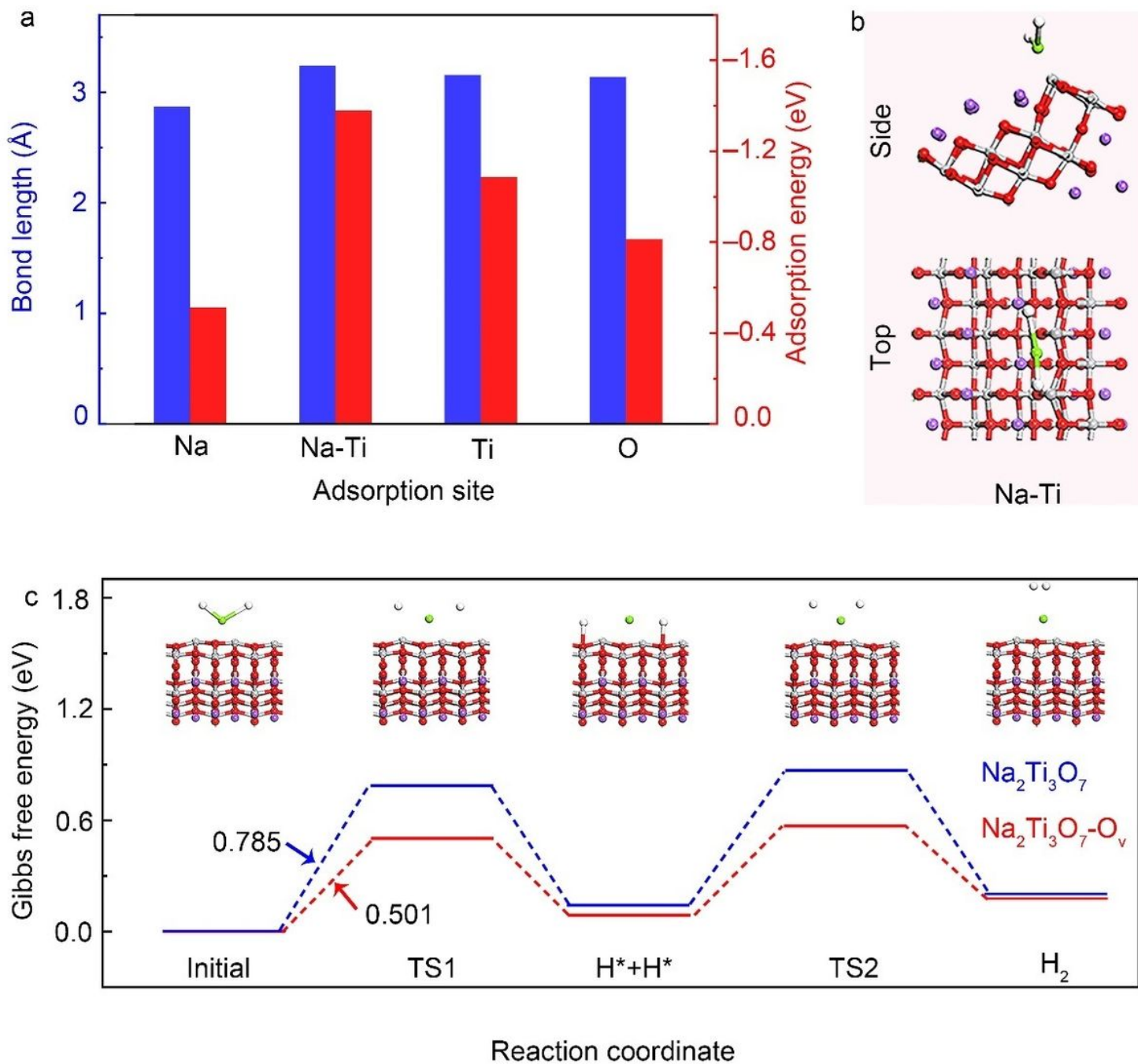


Figure 4

DFT calculations: (a) The adsorption energy (E_{ads}) and bond lengths of Mg-H at different active sites on the MgH₂ + 5Na₂Ti₃O₇-O_v (101) surface; (b) the optimal adsorption structures for MgH₂ molecule at the Na-Ti active sites; (c) The energy profiles of the dissociation and decomposition of MgH₂ molecule on the MgH₂ + Na₂Ti₃O₇ and MgH₂ + Na₂Ti₃O₇-O_v composites as well as the corresponding model structures.

Supplementary Files

This is a list of supplementary files associated with this preprint. Click to download.

- [FinalSMCommunicationsMaterials.doc](#)
- [GraphicAbstract.pdf](#)